

PHYSICS

Origin of micrometer-scale dislocation motion during hydrogen desorption

Motomichi Koyama^{1*†}, Seyedeh Mohadeseh Taheri-Mousavi^{2,3*†}, Haoxue Yan², Jinwoo Kim², Benjamin Clive Cameron⁴, Seyed Sina Moeini-Ardakani⁴, Ju Li^{2,5}, Cemal Cem Tasan^{2*}

Hydrogen, while being a potential energy solution, creates arguably the most important embrittlement problem in high-strength metals. However, the underlying hydrogen-defect interactions leading to embrittlement are challenging to unravel. Here, we investigate an intriguing hydrogen effect to shed more light on these interactions. By designing an in situ electron channeling contrast imaging experiment of samples under no external stresses, we show that dislocations (atomic-scale line defects) can move distances reaching 1.5 μm during hydrogen desorption. Combining molecular dynamics and grand canonical Monte Carlo simulations, we reveal that grain boundary hydrogen segregation can cause the required long-range resolved shear stresses, as well as short-range atomic stress fluctuations. Thus, such segregation effects should be considered widely in hydrogen research.

INTRODUCTION

Hydrogen (H) has been reasoned to cause embrittlement problem in high-strength metallic materials for more than a century (1, 2). H embrittlement is troubling some of the largest industries in existence, which operate in H-abundant environments (e.g., oil and gas, aerospace, defense, automotive), and it has motivated immense scientific research efforts (e.g., ~2000 papers only since 2010).

There are two main factors that cause H to trigger embrittlement. First, H absorption and diffusion can be extremely fast in metals even at room temperature, since it is the lightest element in the universe (i.e., H atomic radius is only ~1/3 of Fe, Ti, or Ni atoms) (3). Second, H embrittlement can be triggered even when the total H uptake is in parts per million (ppm) levels (4). These two factors and the defect-governed nature of metal plasticity and fracture have led to a wide spectrum of investigations on H segregation effects in vacancies (5–7), dislocations (5, 8), and interfaces (6, 9, 10). Among the resulting theories that address HE, the H-enhanced localized plasticity (HELP) theory has generated the most intense discussions (8, 11–21). According to the HELP theory, H causes more localized plastic deformation by enhancing dislocation mobility. The original explanation for the HELP phenomenon is through a proposed H influence on dislocation stress fields (17). The strongest evidence for such a mechanism was provided through in situ environmental transmission electron microscopy (TEM) experiments demonstrating dislocation motion at the crack tip of H-charged samples (22, 23). Notably, these samples were externally stressed. Other researchers reported slip traces induced by H-charging (19, 21). The dislocation activity therein was proposed to be due to microstructural residual

stresses. The authors proposed that the residual stresses could reach levels sufficient for triggering dislocation activity since H-charging may induce reduction in dislocation activation stress (20, 24, 25). Such an interplay between local residual stresses and H effect on the dislocation activation stress (threshold) would explain why such dislocation mobility effects are not more regularly observed and reported: After all, the level of residual stress or H segregation (which are both challenging to measure experimentally) not only varies depending on metal processing and H-charging conditions but also changes as a function of spatial variation of microstructure even in the same material. Yet, such H effects to facilitate dislocation mobility were not confirmed by atomistic simulations (that are not influenced by such experimental challenges) (5, 8), which instead revealed H-induced dislocation pinning (5). The origin of the dislocation activity induced by H-charging thus remains unclear. To move forward, and to explain such discrepancies, experiments with better-controlled boundary conditions are needed, which isolate H-induced microstructural stresses from stresses arising from other factors, e.g., processing residual stresses and external stresses.

Here, to this end, we designed a dedicated experimental methodology to investigate the H effect on dislocation motion, to help shed more light on the nature of such interactions. This experimental procedure is shown in Fig. 1. For these experiments, a face-centered cubic (fcc) iron-manganese (Fe-Mn)-based high-entropy alloy (details in Materials and Methods) was selected. Fcc structure ensures slow desorption rates during the scanning electron microscopy (SEM) experiment. The specimen was mechanically polished to a colloidal silica finish and then cathodically charged with H for 3 hours at 294 K. Considering the diffusion coefficient for austenitic steel [$2.7 \times 10^{-16} \text{ m}^2/\text{s}$ (26)] and the charging time, the depth of the H-affected zone is calculated to be ~2 μm . Right after H-charging, the specimen was briefly repolished with colloidal silica before it was placed in the SEM chamber. Expectedly, exposing the specimen to vacuum in the SEM chamber causes H desorption from the sample (3). During H desorption, we observed dislocation relaxation and motion using the electron channeling contrast imaging (ECCI) technique, which is discussed in detail next.

¹Institute for Materials Research, Tohoku University, 2-1-1 Katahira, Aoba-ku, Sendai 980-8577, Japan. ²Department of Materials Science and Engineering, Massachusetts Institute of Technology, 77 Massachusetts Avenue, Cambridge, MA 02139, USA.

³Department of Mechanical Engineering, Massachusetts Institute of Technology, 77 Massachusetts Avenue, Cambridge, MA 02139, USA. ⁴Department of Civil and Environmental Engineering, Massachusetts Institute of Technology, 77 Massachusetts Avenue, Cambridge, MA 02139, USA. ⁵Department of Nuclear Science and Engineering, Massachusetts Institute of Technology, 77 Massachusetts Avenue, Cambridge, MA 02139, USA.

*Corresponding author. Email: tasan@mit.edu (C.C.T.); smousavi@mit.edu (S.M.T.-M.); koyama@imr.tohoku.ac.jp (M.K.)

†These authors contributed equally to this work.

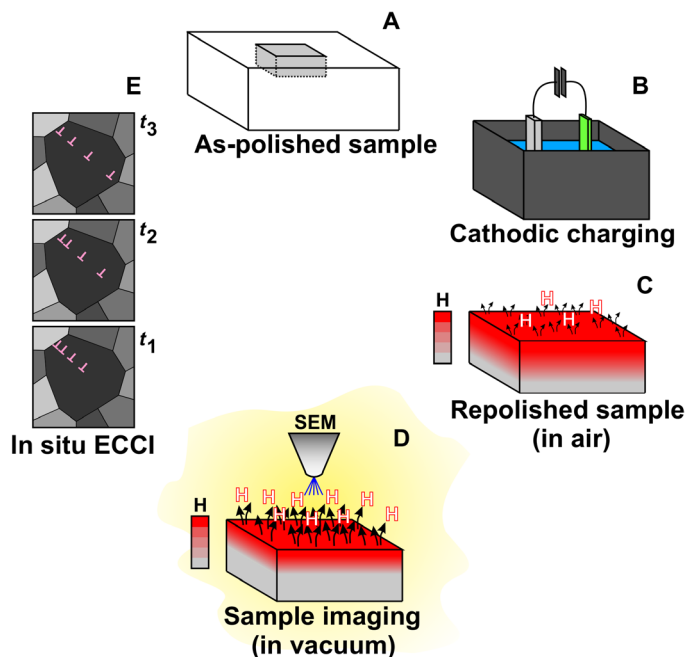


Fig. 1. The experimental procedure that revealed dislocation motion during hydrogen desorption. (A to E) Stages in the experiment.

RESULTS

Experimental observation of dislocation motion during H desorption

Typical results of our experiments are shown in Fig. 2. These tests on the fcc Fe-Mn-based alloy revealed motion of dislocations over large distances ($>1.5 \mu\text{m}$), triggered solely by removing diffusible H from the sample. An example of this phenomenon is shown in Fig. 2A. Here, in the series of ECCI micrographs, as H desorbs out of the sample surface, the increase of the spacing in a planar dislocation array is seen. For clarity, each dislocation is labeled with a letter, and a movie of the dislocation motion is provided online (see movie S1). The largest spacing change takes place after 2 hours (Fig. 2A, third and fourth images), as shown schematically in Fig. 2B. We also provide the full quantitative evolution of the dislocation spacing in this array in Fig. 2C. Several similar observations are made investigating this material further—see Fig. 2 (D to F) for three other zones where rearrangement or disappearance of dislocations in pileups or entanglements are observed (see movies S2 to S4). More examples from this Fe-Mn alloy can be seen in fig. S1 and movie S5. To explore the generality of the observation of dislocation motion, similar experiments were performed on a duplex stainless steel (details in Materials and Methods). Dislocation activities (rearrangements and slip-step formations) can be seen in the austenite phase as shown in fig. S2 and movie S6.

Two characteristics of these results need to be emphasized, in comparison to earlier studies on dislocation motion due to H-charging (15, 23, 27). First, the experiments presented here were specifically designed to minimize the influence of other effects that could cause dislocation motion. There were no externally applied heat or stresses. Similarly, there were no beam heating effects, since the experiments are carried out at room temperature using the SEM-based ECCI method (28, 29). To further ensure that the observed dislocation motions are not driven by surface stresses due to preparation or

stresses from the electron beam, control experiments were conducted on samples without H-charging. The dislocations remain immobile (see fig. S3), indicating that the ECCI technique and the presented sample preparation method are not the causes of the observed dislocation activity. Furthermore, there were no TEM sample preparation artifacts (that arise, e.g., due to focused ion beam milling), since ECCI enables imaging of surface dislocations in bulk samples. The experiment did not trigger any phase transformations, since this alloy has a stable microstructure (30). Second, the observed glide distances are larger [from ~ 3 times (15, 22) to ~ 2 orders of magnitude (15, 23)] than those reported in previous studies in the literature where a similar H-induced phenomenon was observed.

Numerical simulations investigating the origin of the dislocation mobility

To study the origin of the driving force for the observed dislocation motion, we first investigated the possibility of surface high concentration of H inducing dislocation motion by creating sufficiently high shear stresses. To this end, we calculated the maximum level of stresses that can be generated, by assuming the extreme condition that only the surface expands due to large H content segregation. In this case, the compressive stress along the surface of the sample is equivalent in all directions and equal to $\sigma = \frac{-E w c}{1-\nu}$ (31). The stress perpendicular to the surface is zero as it can freely expand in this direction. By considering $E = 200 \text{ GPa}$ for the Young's modulus, $w = 2 \times 10^{-6} \text{ m}^3/\text{mol}$ for the molar expansion (32), $c \sim 3 \text{ mol/m}^3$ for H concentration calculated for our experiment at the sample surface, and $\nu = 0.3$ for the Poisson ratio of the material, the maximum shear stress occurring at 45° with respect to the sample surface is obtained as $\sim 1 \text{ MPa}$. This value is at least one order of magnitude below the required activation stress for dislocation glide, which indicates that the surface expansion due to the uniform increase in H concentration cannot be the main factor causing the observed dislocation motion in the experiments. The H distribution needs to be nonuniform to achieve higher stress magnitudes.

Next, we conducted hybrid molecular dynamics (MD)/grand canonical Monte Carlo (GCMC) simulations to investigate the fundamentals of the competition among different microstructural constituents [e.g., grain boundaries (GBs) and dislocations] to act as potential sites for H segregation. Using the GCMC algorithm enables bridging the time scale limitations of MD simulations, which is necessary to capture microstructural H diffusion tendencies. As in the case of the experiments, when designing these simulations, the factors that can influence these tendencies need to be strategically minimized. As the resolved stress required for dislocation motion can be influenced by stochastic interactions of the present dislocations with randomly distributed substitutional alloying elements (33), a pure metal was chosen for simulations, which exhibits fcc crystal structure (as in the experiments). Note, however, that pure Fe at room temperature exhibits body-centered cubic structure, and stabilization of fcc Fe requires alloying of nickel (Ni), manganese, carbon, or other austenite stabilizers. Also, for such multicomponent Fe-based fcc alloys containing H, currently reliable interatomic potentials do not exist. Therefore, to elucidate the fundamentals of the underlying mechanisms, we conducted simulations on pure Ni, for which the interatomic potential is available for atomistic-scale simulations (18, 34). Note that Ni is the nearest fcc metal to Fe in the periodic table; thus, it has minimal difference in the atomic size and in the stress due to the presence of H in the interstitial sites or at GB (free volume sites).

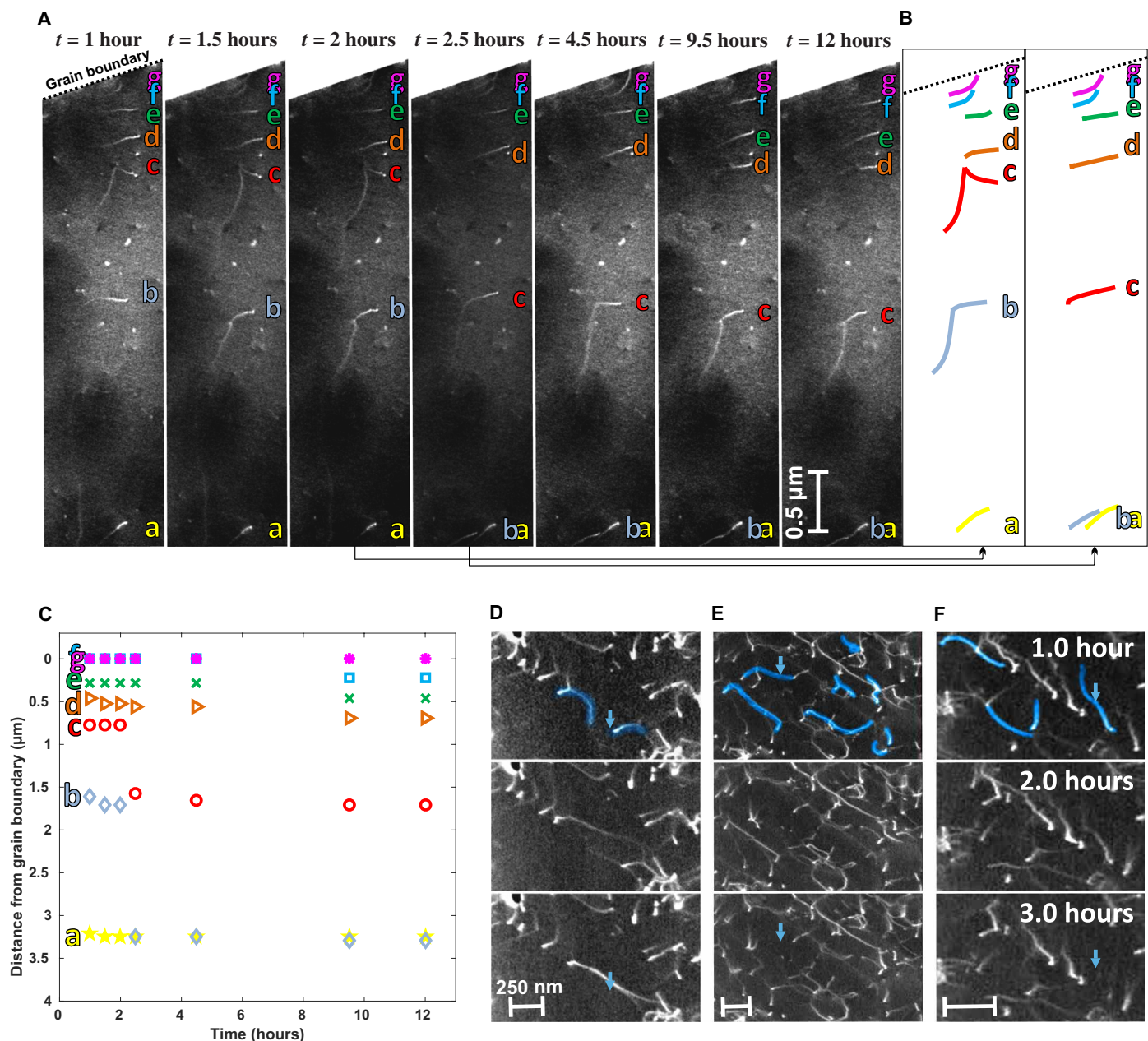


Fig. 2. Dislocation motion during H desorption in Fe-Mn-based alloy captured by ECCI. (A) A planar dislocation pileup at a grain boundary (GB) at different stages of H desorption. (B) Dislocation configurations at $t = 2$ and 2.5 hours are shown schematically. Note the $\sim 1.5\text{-}\mu\text{m}$ distance that dislocations b and c glide. (C) Relative positions of dislocations with respect to the GB are plotted against exposure time. (D to F) Three other examples of H desorption-induced dislocation motion are presented. The blue color indicates dislocations that are most strongly affected. Movies are available online.

A three-dimensional (3D) polycrystalline sample with a grain size of 7.5 nm was modeled (see fig. S4). A total deformation strain of 10% was applied to produce a dislocation network. Then, two simulations were performed on this prestrained sample. In the first one, H atoms were inserted in the sample using hybrid MD/GCMC simulations for 6 ns. The H atomic ratio was increased to 0.45 atomic % (at %) in the sample excluding free surfaces. This percentage is identical to the H percentage in the experimental samples (see fig. S5). For the second simulation and as a reference, the prestrained simulation box was relaxed for 6 ns, and the dislocation network was traced for comparison to the H-charged sample. Application of

the hybrid MD/GCMC technique results in a hydrogenated sample in chemical equilibrium for a given H_2 chemical potential/partial pressure, in which, for example, the same H percentage migrates from GBs to the free surface and vice versa. Moreover, due to the application of the GCMC technique, no preassumption about the location of H is required, and the energetically favorable sites are chosen by the algorithm automatically. The simulation details are provided in Materials and Methods.

As seen in the 3D view in Fig. 3A, and more clearly in Fig. 3B, which is a 2D slice from the H-charged sample, H atoms exhibit a nonuniform distribution: They are mainly located on free surfaces

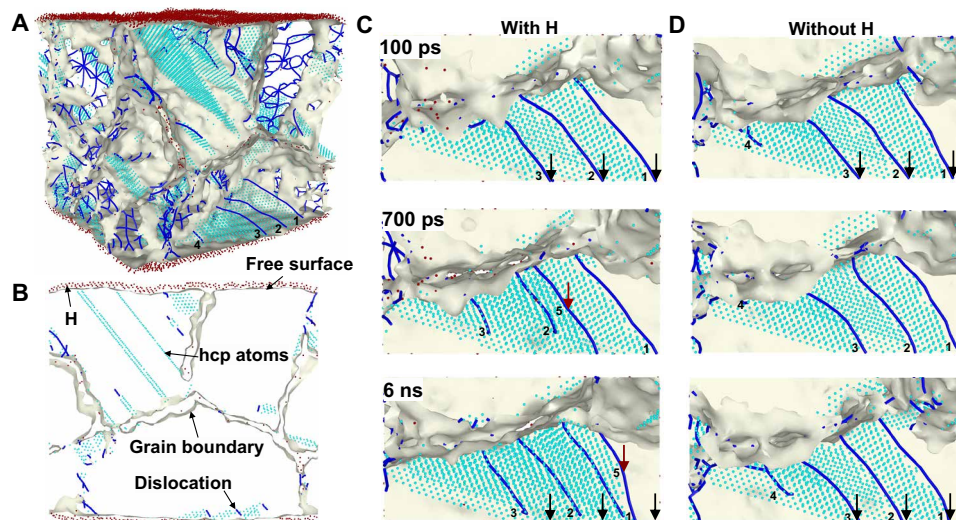


Fig. 3. Atomistic simulation of dislocation motion during H-charging in Ni polycrystalline sample. Hybrid MD/GCMC simulations reveal that H mainly segregates at GBs and free surfaces, as shown in (A) 3D and (B) 2D views. Here, gray zones represent GBs, red spheres are H atoms, light blue atoms are hexagonal close-packed (hcp) atoms, and dark blue lines are the dislocation network. Snapshots of the dislocation structures in H-charged samples shown in (C) reveal clear dislocation rearrangements (see the black arrows). The red arrows point out a new dislocation generated during H-charging of the sample (see movie S7). H-free sample in (D) shows little dislocation activity.

and GBs. Observations of H segregation in GBs were reported in various investigations, for example, by using cryo-transfer atom probe tomography (35) or by silver-decoration experiments (36, 37), carried out with various metals including Fe and Ni. An important consequence of these results in Fig. 3 (and the mentioned supporting experimental evidence) is regarding direct effects of H on dislocations: As H atoms prefer to stay in GBs rather than dislocations, they impose little pinning effect on dislocation motion (5). Thus, present dislocations in our simulations move without constraint in the sample. The snapshots of a dislocation network in a grain of a H-charged and a H-free sample are shown in Fig. 3 (C and D, respectively) (see movies S7 and S8). A comparison of these two figures reveals that after 700 ps, the spacing between dislocations 1 to 3 increases as a newly generated dislocation 5 moves in the H-charged sample, similar to the experimental observations shown in Fig. 2. As dislocation 5 moves forward in the grain, the stress distribution changes and the dislocations in the pileup rearrange once more. The H-free sample, on the other hand, exhibits relatively less dislocation activity both in the shown region and elsewhere in the sample.

We next computationally investigate the underlying mechanisms for the rearrangement of dislocations seen experimentally in Fig. 2 and computationally in Fig. 3C. In these simulations, an undeformed polycrystalline Ni sample is charged with H to the same H percentage as in the experiment. The atomic-level von Mises stress distribution of the H-charged sample is shown in Fig. 4A. The contour is the temporal average of the stress for each atom over 6 ns. The calculation method of the von Mises stress is presented in Materials and Methods. Higher stress levels are observed on GBs, compared to the bulk of the grains. The atomic-level von Mises stress distributions of the atoms in the bulk (grain interiors) and in the GBs before and after H-charging are plotted in Fig. 4B. To verify the stability of the presented curves, the temporal average was calculated over different time periods. Figure 4C shows that the temporal average saturates by increasing the averaging time period. For example, it is seen that the curve of 6 ns has a shift of less than 5 MPa with respect to the curve of 5.5 ns averaging time. The saturation indicates that the stress

fluctuation due to atomic vibrations is not significant, and the average value is the decisive parameter.

The von Mises stress in Fig. 4B spans from zero to tens of gigapascals in both the GBs and the bulk of the sample. These high values compared to the experimentally measured yield strength values (on the order of megapascals) may raise questions on physical validity of these atomic-level stresses. It should be noted, however, that at nanoscale, the crystal can tolerate stress magnitude up to the ideal shear strength (on the order of $1/10$ of shear modulus $G/10$) (38, 39), which can be three orders of magnitude higher than the macroscopic stress values measured by testing highly defected polycrystals.

In Fig. 4B, the bottom inset shows that H segregation at GBs imposes a change of ~ 200 MPa in von Mises stress of atoms located in GBs. This level of change can influence dislocation emissions from GBs, the structure of the already absorbed dislocations in GBs (40), and, more importantly, the dislocation interactions near GBs. For example, Fig. 4B demonstrates that the induced long-range stress effect can reach ~ 200 MPa on bulk atoms, near the boundaries. We have also plotted the von Mises stress of individual atoms before and after H-charging in the sample. This plot also presents a change of 150 to 200 MPa in the stress due to the H-charging of the sample (see fig. S6). Stresses at this level should not only induce dislocation activity but also cause local variation of crystallographic orientation near boundaries. This was validated by our in situ electron back-scattered diffraction analysis during H-charging of duplex stainless steel (see fig. S7). The observed increase in point-to-point misorientation angle along the phase boundary during H-charging may reflect the localized stress induced by H segregation at the boundary.

In Fig. 4 (B and C), the change in von Mises stress is presented; however, what actually relocates dislocations in the crystal is the resolved shear stress along the slip direction. Therefore, the change of shear stress due to H, directly on two arbitrary slip directions of the Ni crystal, was also investigated for three representative GBs ($\Sigma 9$, $\Sigma 41c$, and $\Sigma 99b$) (see fig. S8). As seen in fig. S9, the shear stress varies depending on the slip direction and GB type (i.e., between 50 and 200 MPa). This clarifies why dislocation activity due to H-charging

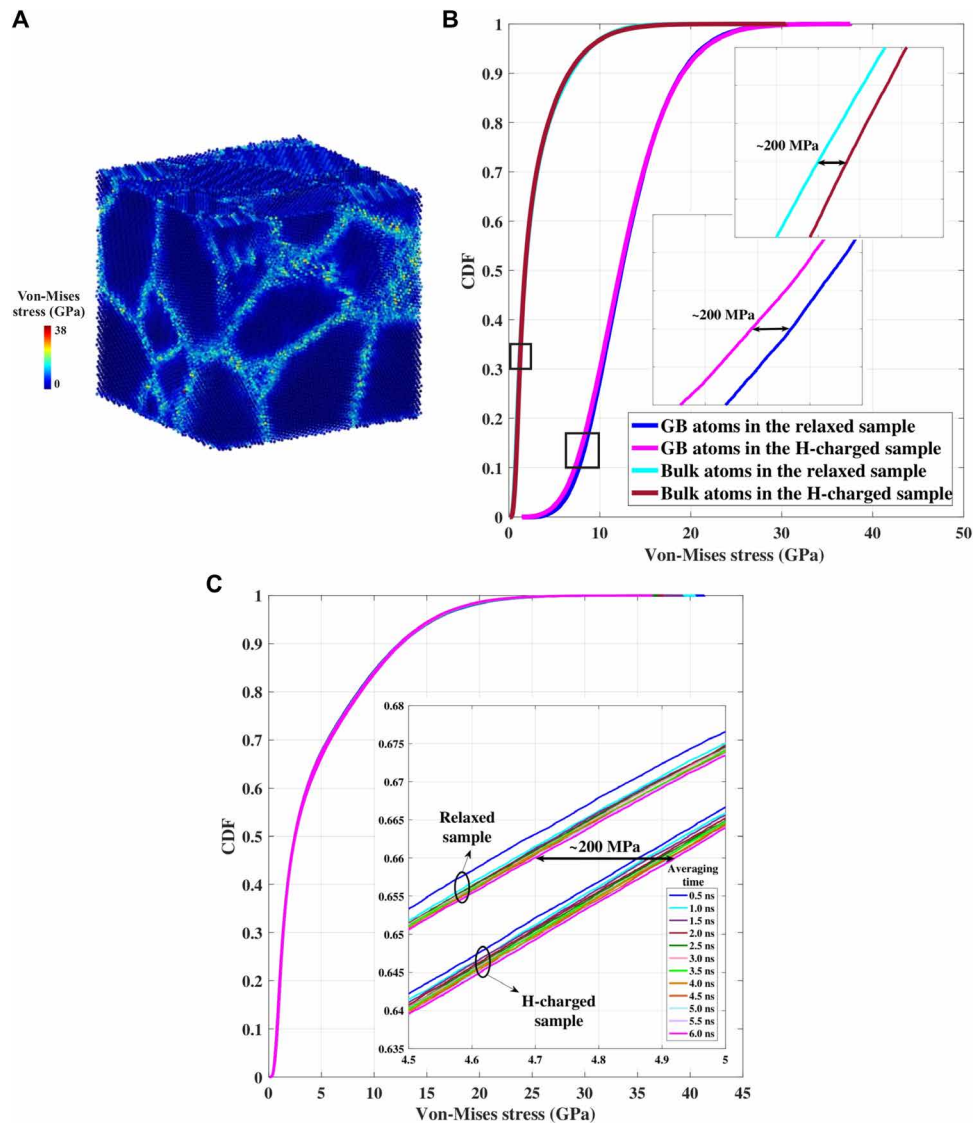


Fig. 4. Atomic-level von Mises stress distribution due to hydrogen diffusion in polycrystalline Ni sample. (A) Atomic-level von Mises stress distribution from atomistic simulation. The stress has a higher magnitude on GBs. (B) The cumulative density function (CDF) of von Mises stress distribution of atoms in grain interiors (bulk) and GBs before and after H-charging into the sample. The two insets are the zoomed windows showing 200 MPa change in von Mises stress of atoms in bulk and GBs, due to H-charging into the sample. (C) The temporal average of the von Mises stress for different averaging time periods ranging from 500 ps to 6 ns. The temporal average converges by increasing the averaging time period.

or desorption should not be expected to be at the same level near every GB. The resolved shear stress is highly dependent on the GB type and also the slip direction. This point once more underlines the importance of experimenting with and simulating polycrystalline samples, to be able to embrace the stochasticity of this problem. Under a given H_2 partial pressure, only a certain percentage of dislocations will be relocating, which is highly dependent on several influential parameters such as the GB orientation, slip systems, dislocation type, dislocation density, and residual stress due to dislocation interactions with other dislocations and microstructural features.

DISCUSSION

These results altogether reveal that it is the shear stress arising from H segregation at boundaries that drives the experimentally observed

dislocation activity (Fig. 2 and figs. S1 and S2). They also shed light on the intrinsic challenges in observing and understanding this effect computationally and experimentally. Earlier computational investigations on H influence on dislocation mobility, for example, did not capture the effect shown here, as those models did not explicitly include GBs where H could segregate (5, 8). The main challenge experimentally, on the other hand, is systematic control of all factors that can alter the apparent H effect on dislocations. The H segregation-induced stress can itself cause dislocation motion as shown here; however, in some cases, it would have to act against residual stresses already existing in the microstructure due to the processing. The resulting observable H effect will thus depend not only on whether the H-charging or desorption can adequately supply the change in local shear stress required for dislocation activity but also on the sign and the level of local stress landscape before the

introduction of H. Since both microstructural residual stresses and H diffusion kinetics are influenced by local variations in grain crystallographic orientation, shape, anisotropy, composition, GB characteristics, and other microstructural characteristics, the resulting dislocation activity may vary significantly, e.g., from atomic-scale rearrangements to micrometer-scale motions. We argue that, due to the same reasoning, different levels of dislocation activity can be seen in a single sample or even in a single grain at different distances to a given boundary (e.g., fig. S1). Dislocations in the pileup shown in Fig. 2A demonstrates an example of this variation: The motion of dislocations at the pileup core (g, f, e) are more restricted under higher pileup stress [e.g., requiring higher resolved shear stress (41), and relocation of pressing dislocations (a, b, c) to open up the space for their movements, etc.], and thus their motion remains relatively limited (detection of which is at the limits of ECCI) compared to the dislocations further away from the boundary. This is despite the expectation that the stress due to H segregation must be highest near the GB.

To further understand the dependency of H segregation-induced stresses to these effects, new experimental methods that are capable of mapping large fields of view with high spatial resolution are required to correlate crystallographic defects, H, and residual stress distributions in a statistically relevant manner. Similarly, new investigations are called for to investigate these phenomena away from the surface. The observations presented in this work are from surface grains, yet the same effect is expected to be present in the subsurface grains, near GBs, and especially at triple junctions. Unfortunately, direct imaging of the dislocation activity at these subsurface areas, during H-charging or desorption, is experimentally challenging (if at all possible). Nevertheless, as a first attempt, by using an in-house designed and built H-charging setup, we carried out an in situ synchrotron diffraction experiment during H-charging, which revealed crystallographic reorientations of the investigated bulk fcc grains (fig. S10). While this does serve as an indirect supporting evidence for the induced stress effects due to H-charging in the bulk of the sample, more investigations are required to further improve our understanding of these processes away from the sample surfaces.

In summary, we carefully designed an experimental procedure to study the H-influence on dislocation mobility in polycrystalline samples. Our in situ ECCI imaging analysis revealed that the desorption of H atoms from the investigated fcc alloys caused micrometer-scale dislocation motion on the sample surface. Our hybrid MD/GCMC simulations revealed that the driving force for dislocation movement is provided by the high stress concentration arising from H segregation at GBs. This insight regarding the dislocation movements in the H-charged polycrystalline samples without external loading will shed more light on the apparent enhanced plasticity in hydrogen presence reported by multiple researchers. These results also call for a broad range of follow-up investigations since GB-H interactions can lead to a wide range of local stress distributions and, in turn, critical macromechanical effects.

MATERIALS AND METHODS

H-charging of Fe-Mn-based alloy

The H-charging for the Fe-Mn-based alloy was performed at 10 A/m^2 for 3 hours in a solution of 5% H_2SO_4 with NH_4SCN (3 g/liter). In this study, two alloys Fe-20Mn-30Ni-6Co-2Cr (Fig. 2A) and Fe-30Mn-30Ni-6Co-2Cr (Fig. 2D and fig. S1) (at %) were used for the experiments, respectively.

The ECCI technique was carried out at an acceleration voltage of 30 kV and a beam size of 4 nm. To determine the diffusible H content, thermal desorption mass spectrometry (TDS) was conducted. The H-charged specimen was first exposed to ambient temperature for 24 hours in the TDS chamber under vacuum to estimate the desorbed H amount from the H-affected zone during the in situ ECCI experiments. The H-affected zone volume was estimated by specimen surface area (0.86 cm^2) and the depth of the H-affected zone ($\sim 2 \mu\text{m}$). Note here that the H-affected depth is estimated through H diffusion distance from the surface \sqrt{Dt} , where D is the H diffusion coefficient of an austenitic steel at 294 K ($2.74 \times 10^{-16} \text{ m}^2/\text{s}$) and t is the H-charging time. The diffusible H estimated for the H-affected zone volume was 0.45 at %. After ambient temperature aging, the specimen was then heated up to 600 K at a heating rate of 400 K/hour. The total diffusible H content for the total specimen includes the diffusible H desorbed during the ambient temperature aging and during TDS heating up to 473 K [where the first TDS peak ended (see fig. S5)]. The diffusible H content for the total specimen was estimated to be 14 at. ppm.

H-charging of duplex stainless steel

The H-charging for duplex stainless steel alloy was carried out at 10 A/m^2 for 2 hours in a solution of 3% NaCl with NH_4SCN (3 g/liter) for the desorption ECCI observation experiment. The specimen was mechanically polished to a colloidal silica finish. Right after H-charging, the specimen was briefly repolished with colloidal silica again before being placed in the SEM chamber, where H desorption is continuous due to vacuum. The ECCI was carried out at an acceleration voltage of 20 kV and a working distance of 3.1 mm.

Synchrotron diffraction during H-charging of duplex stainless steel

Duplex stainless steel sample was tested under transmission mode of synchrotron diffraction at the 11-ID-C beamline of the Advanced Photon Source of Argonne National Laboratory. The polycrystalline sample was 0.575 mm thick, the beam size was $0.8 \times 0.8 \text{ mm}^2$, and the beam energy was 105.7 keV ($\lambda = 0.1174 \text{ \AA}$). In situ cathodic H-charging was carried out using an electrolyte of 1 M H_2SO_4 with NH_4SCN (5 g/liter) recombination poisoner at a current density of 5 A/m^2 .

Hybrid MD/GCMC simulations

A 3D polycrystalline Ni sample with dimensions of 15 nm by 15 nm by 15 nm was prepared. The sample contained eight randomly oriented grains with a mean grain size of $d = 7.5 \text{ nm}$ and approximately 300,000 atoms. While considering 2.5-nm vacuum at the Z direction, periodic boundary conditions were imposed at the X and Y boundaries of the sample. The vacuum surface was chosen owing to the similar boundary condition in the experimental sample (see Fig. 1A). MD and GCMC simulations were performed using an in-house library (42) and the Large-scale Atomic/Molecular Massively Parallel Simulator (LAMMPS) code (43). The embedded atom method potential was adapted for Ni (and, when needed, Ni-H) interatomic interactions (44), and the Nose-Hoover thermostat was used to maintain the NPT ensemble at the ambient temperature $T = 300 \text{ K}$. The integration time steps for the system with and without H were considered as 0.5 and 1 fs, respectively. The sample was initially relaxed at 300 K for 500 ps in an NPT ensemble. Dislocation network was generated in the sample by applying a 10% tensile deformation along

the X direction. The strain rate was 10^9 s^{-1} . Hybrid MD/GCMC simulations on NVT and μVT ensembles were conducted and H atoms were therefore inserted in and extracted from the sample. H chemical potential was -2.462 eV . Every 0.5 ps, 10,000 GCMC trials were carried out, and the H concentration was raised to 0.45 at % after 6 ns. To certify a similar result under different H introduction, several insertion procedures were tested, and an identical H concentration was obtained. Dislocation configuration in the H-charged sample was compared to that in a prestrained sample, which was relaxed for 6 ns in an NVT ensemble.

To analyze the von Mises stress before and after H-charging, an undeformed polycrystalline sample was relaxed at 300 K for 6 ns and the temporal average of von Mises stress for the atoms in GBs and grain interiors (bulk) was calculated over increasing time periods from 500 ps to 6 ns to monitor the stability of the average stress distribution. H atoms were then inserted in the relaxed sample every 0.5 ps, as 10,000 GCMC trials were conducted. The chemical potential was -2.447 eV to increase the H percentage to 0.45 at % after 2 ns. The sample was then relaxed for 6 ns in an NVT ensemble, and the temporal average of the von Mises stress in GBs and the bulk over increasing time periods was compared to the H-free sample (see Fig. 4C).

The evolution and distribution of dislocations were monitored using the dislocation analysis modifier (DXA) of the OVITO program (45). In the adopted atom coloring scheme, gray stands for fcc atoms, light blue stands for hexagonal close-packed, and purple stands for atoms in GBs. H atoms are colored red.

SUPPLEMENTARY MATERIALS

Supplementary material for this article is available at <http://advances.sciencemag.org/cgi/content/full/6/23/eaaz1187/DC1>

REFERENCES AND NOTES

- W. H. Johnson, II. On some remarkable changes produced in iron and steel by the action of hydrogen and acids. *Proc. R. Soc. Lond.* **23**, 168–179 (1874).
- Y. Fukai, *The Metal-Hydrogen System: Basic Bulk Properties* (Springer, 2005).
- R. W. Balluffi, S. M. Allen, W. C. Carter, *Kinetics of Materials* (John Wiley & Sons Inc., 2005).
- M. Koyama, M. Rohwerder, C. C. Tasan, A. Bashir, E. Akiyama, K. Takai, D. Raabe, K. Tsuzaki, Recent progress in microstructural hydrogen mapping in steels: Quantification, kinetic analysis, and multi-scale characterisation. *Mater. Sci. Technol.* **33**, 1481–1496 (2017).
- D. Xie, S. Li, M. Li, Z. Wang, P. Gumbsch, J. Sun, E. Ma, J. Li, Z. Shan, Hydrogenated vacancies lock dislocations in aluminium. *Nat. Commun.* **7**, 13341 (2016).
- T. Hickle, R. Nazarov, E. J. McEniry, G. Leyson, B. Grabowski, J. Neugebauer, Ab initio based understanding of the segregation and diffusion mechanisms of hydrogen in steels. *JOM* **66**, 1399–1405 (2014).
- G. Lu, E. Kaxiras, Hydrogen embrittlement of aluminum: The crucial role of vacancies. *Phys. Rev. Lett.* **94**, 155501 (2005).
- J. Song, W. A. Curtin, Mechanisms of hydrogen-enhanced localized plasticity: An atomistic study using α -Fe as a model system. *Acta Mater.* **68**, 61–69 (2014).
- A. Tehranchi, W. A. Curtin, Atomistic study of hydrogen embrittlement of grain boundaries in nickel: I. Fracture. *J. Mech. Phys. Solids.* **101**, 150–165 (2017).
- J. Song, W. A. Curtin, Atomic mechanism and prediction of hydrogen embrittlement in iron. *Nat. Mater.* **12**, 145–151 (2013).
- Y. Gu, J. A. El-Awady, Quantifying the effect of hydrogen on dislocation dynamics: A three-dimensional discrete dislocation dynamics framework. *J. Mech. Phys. Solids* **112**, 491–507 (2018).
- H. Luo, Z. Li, Y.-H. Chen, D. Ponge, M. Rohwerder, D. Raabe, Hydrogen effects on microstructural evolution and passive film characteristics of a duplex stainless steel. *Electrochem. Commun.* **79**, 28–32 (2017).
- L. Claeys, T. Depover, I. DeGraeve, K. Verbeken, Electrochemical hydrogen charging of duplex stainless steel. *Corrosion* **75**, 880–887 (2019).
- I. M. Robertson, P. Sofronis, A. Nagao, M. L. Martin, S. Wang, D. W. Gross, K. E. Nygren, Hydrogen embrittlement understood. *Metall. Mater. Trans. B.* **46**, 1085–1103 (2015).
- I. M. Robertson, The effect of hydrogen on dislocation dynamics. *Eng. Fract. Mech.* **68**, 671–692 (2001).
- P. Sofronis, Y. Liang, N. Aravas, Hydrogen induced shear localization of the plastic flow in metals and alloys. *Eur. J. Mech. A Solids.* **20**, 857–872 (2001).
- H. K. Birnbaum, P. Sofronis, Hydrogen-enhanced localized plasticity—A mechanism for hydrogen-related fracture. *Mater. Sci. Eng.* **176**, 191–202 (1994).
- A. Tehranchi, B. Yin, W. A. Curtin, Softening and hardening of yield stress by hydrogen-solute interactions. *Philos. Mag.* **97**, 400–418 (2016).
- G. Lu, Q. Zhang, N. Kioussis, E. Kaxiras, Hydrogen-enhanced local plasticity in aluminum: An ab initio study. *Phys. Rev. Lett.* **87**, 095501 (2001).
- A. Barnoush, H. Vehoff, Recent developments in the study of hydrogen embrittlement: Hydrogen effect on dislocation nucleation. *Acta Mater.* **58**, 5274–5285 (2010).
- A. Barnoush, M. Zamanzade, H. Vehoff, Direct observation of hydrogen-enhanced plasticity in super duplex stainless steel by means of in situ electrochemical methods. *Scr. Mater.* **62**, 242–245 (2010).
- D. S. Shih, I. M. Robertson, H. K. Birnbaum, Hydrogen embrittlement of α titanium: In situ TEM studies. *Acta Metall.* **36**, 111–124 (1988).
- P. J. Ferreira, I. M. Robertson, H. K. Birnbaum, Hydrogen effects on the interaction between dislocations. *Acta Mater.* **46**, 1749–1757 (1998).
- A. Barnoush, B. Yang, H. Vehoff, Effect of hydrogen and grain boundaries on dislocation nucleation and multiplication examined with a Ni-AFM, in *Advances in Solid State Physics* (Springer Berlin Heidelberg, 2008), pp. 253–269.
- H. Luong, M. R. Hill, The effects of laser peening and shot peening on high cycle fatigue in 7050-T7451 aluminum alloy. *Mater. Sci. Eng. A* **527**, 699–707 (2010).
- T.-P. Perng, C. J. Altstetter, Effects of deformation on hydrogen permeation in austenitic stainless steels. *Acta Metall.* **34**, 1771–1781 (1986).
- D. P. Abraham, C. J. Altstetter, Hydrogen-enhanced localization of plasticity in an austenitic stainless steel. *Metall. Mater. Trans. A.* **26**, 2859–2871 (1995).
- I. Gutierrez-Urrutia, S. Zaeferrer, D. Raabe, Electron channelling contrast imaging of twins and dislocations in twinning-induced plasticity steels under controlled diffraction conditions in a scanning electron microscope. *Scr. Mater.* **61**, 737–740 (2009).
- S. Zaeferrer, N.-N. Elhami, Theory and application of electron channelling contrast imaging under controlled diffraction conditions. *Acta Mater.* **75**, 20–50 (2014).
- Z. Li, K. G. Pradeep, Y. Deng, D. Raabe, C. C. Tasan, Metastable high-entropy dual-phase alloys overcome the strength–ductility trade-off. *Nature* **534**, 227–230 (2016).
- A. F. Bower, *Applied Mechanics of Solids* (Taylor & Francis, 2012); <http://solidmechanics.org/> [accessed 7 August, 2018].
- M. Nagumo, *Fundamentals of Hydrogen Embrittlement* (Springer Singapore, 2016).
- G. P. M. Leyson, W. A. Curtin, L. G. Hector Jr., C. F. Woodward, Quantitative prediction of solute strengthening in aluminium alloys. *Nat. Mater.* **9**, 750–755 (2010).
- J. Song, W. A. Curtin, A nanoscale mechanism of hydrogen embrittlement in metals. *Acta Mater.* **59**, 1557–1569 (2011).
- Y.-S. Chen, H. Lu, J. Liang, A. Rosenthal, H. Liu, G. Sneddon, I. McCarroll, Z. Zhao, W. Li, A. Guo, J. M. Cairney, Observation of hydrogen trapping at dislocations, grain boundaries, and precipitates. *Science* **367**, 171–175 (2020).
- T. Schober, C. Dieker, Observation of local hydrogen on nickel surfaces. *Metall. Trans. A.* **14**, 2440–2442 (1983).
- M. Koyama, D. Yamasaki, T. Nagashima, C. C. Tasan, K. Tsuzaki, In situ observations of silver-decoration evolution under hydrogen permeation: Effects of grain boundary misorientation on hydrogen flux in pure iron. *Scr. Mater.* **129**, 48–51 (2017).
- T. Zhu, J. Li, A. Samanta, A. Leach, K. Gall, Temperature and strain-rate dependence of surface dislocation nucleation. *Phys. Rev. Lett.* **100**, 025502 (2008).
- D. Srolovitz, T. Egami, V. Vitek, Radial distribution function and structural relaxation in amorphous solids. *Phys. Rev. B.* **24**, (1981).
- T. Zhu, J. Li, A. Samanta, H. G. Kim, S. Suresh, Interfacial plasticity governs strain rate sensitivity and ductility in nanostructured metals. *Proc. Natl. Acad. Sci. U.S.A.* **104**, 3031–3036 (2007).
- R. J. Asaro, S. Suresh, Mechanistic models for the activation volume and rate sensitivity in metals with nanocrystalline grains and nano-scale twins. *Acta Mater.* **53**, 3369–3382 (2005).
- S. S. Moeini adrakani, J. Li, *MAPP* (2017); www.mit.edu/~sinam/mapp.
- S. Plimpton, Fast parallel algorithms for short-range molecular dynamics. *J. Comput. Phys.* **117**, 1–19 (1995).
- J. E. Angelo, N. R. Moody, M. I. Baskes, Trapping of hydrogen to lattice defects in nickel. *Model. Simul. Mater. Sci. Eng.* **3**, 289–307 (1995).
- A. Stukowski, Visualization and analysis of atomistic simulation data with OVITO—the Open Visualization Tool. *Model. Simul. Mater. Sci. Eng.* **18**, 015012 (2010).

Acknowledgments

Funding: This work made use of the MRSEC Shared Experimental Facilities at MIT, supported by the NSF under award number DMR-14-19807. M.K. acknowledges the support from JSPS KAKENHI (JP16H06365 and JP20H02457). S.M.T.-M. acknowledges the financial support from the Swiss National Science Foundation through grant P300P2_171423. B.C.C., S.S.M.-A., J.L.,

J.K., and C.C.T. acknowledge the support from the Exelon Corporation—Agreement Effective 4/1/16. J.L. also acknowledges support by NSF CMMI-1922206. The effort from H.Y. is sponsored by the Department of the Navy, Office of Naval Research under ONR award number N00014-18-1-2284. Any opinions, findings, and conclusions or recommendations expressed in this material are those of the author(s) and do not necessarily reflect the views of the Office of Naval Research. The authors acknowledge the MIT SuperCloud and Lincoln Laboratory Supercomputing Center for providing (HPC and consultation) resources that have contributed to the numerical results reported within this paper. **Author contributions:** C.C.T. designed the research. C.C.T. and M.K. designed the experiments. M.K., H.Y., J.K., B.C.C., and C.C.T. performed the experiments. S.M.T.-M., S.S.M.-A., and J.L. designed and performed the simulations. S.M.T.-M., M.K., and C.C.T. co-wrote the manuscript. All authors discussed the results and commented on the manuscript. **Competing interests:** The authors declare that

they have no competing interests. **Data and materials availability:** All data needed to evaluate the conclusions in the paper are present in the paper and/or the Supplementary Materials. Additional data related to this paper may be requested from the authors.

Submitted 13 August 2019

Accepted 14 April 2020

Published 5 June 2020

10.1126/sciadv.aaz1187

Citation: M. Koyama, S. M. Taheri-Mousavi, H. Yan, J. Kim, B. C. Cameron, S. S. Moeini-Ardakani, J. Li, C. C. Tasan, Origin of micrometer-scale dislocation motion during hydrogen desorption. *Sci. Adv.* **6**, eaaz1187 (2020).

Origin of micrometer-scale dislocation motion during hydrogen desorption

Motomichi Koyama, Seyedeh Mohadeseh Taheri-Mousavi, Haoxue Yan, Jinwoo Kim, Benjamin Clive Cameron, Seyed Sina Moeini-Ardakani, Ju Li and Cemal Cem Tasan

Sci Adv 6 (23), eaaz1187.
DOI: 10.1126/sciadv.aaz1187

ARTICLE TOOLS	http://advances.sciencemag.org/content/6/23/eaaz1187
SUPPLEMENTARY MATERIALS	http://advances.sciencemag.org/content/suppl/2020/06/01/6.23.eaaz1187.DC1
REFERENCES	This article cites 38 articles, 2 of which you can access for free http://advances.sciencemag.org/content/6/23/eaaz1187#BIBL
PERMISSIONS	http://www.sciencemag.org/help/reprints-and-permissions

Use of this article is subject to the [Terms of Service](#)

Science Advances (ISSN 2375-2548) is published by the American Association for the Advancement of Science, 1200 New York Avenue NW, Washington, DC 20005. The title *Science Advances* is a registered trademark of AAAS.

Copyright © 2020 The Authors, some rights reserved; exclusive licensee American Association for the Advancement of Science. No claim to original U.S. Government Works. Distributed under a Creative Commons Attribution NonCommercial License 4.0 (CC BY-NC).

Supplementary Materials for

Origin of micrometer-scale dislocation motion during hydrogen desorption

Motomichi Koyama*, Seyedeh Mohadeseh Taheri-Mousavi*, Haoxue Yan, Jinwoo Kim, Benjamin Clive Cameron, Seyed Sina Moeini-Ardakani, Ju Li, Cemal Cem Tasan*

*Corresponding author. Email: tasan@mit.edu (C.C.T.); smousavi@mit.edu (S.M.T.-M.); koyama@imr.tohoku.ac.jp (M.K.)

Published 5 June 2020, *Sci. Adv.* **6**, eaaz1187 (2020)
DOI: 10.1126/sciadv.aaz1187

The PDF file includes:

Legends for movies S1 to S8
Figs. S1 to S10

Other Supplementary Material for this manuscript includes the following:

(available at advances.sciencemag.org/cgi/content/full/6/23/eaaz1187/DC1)

Movies S1 to S8

Movie legends:

Movie S1. Rearrangement of a planar dislocation pile-up at a GB at different stages of H desorption from a Fe-Mn based alloy sample.

Movies S2-S5. H desorption-induced dislocation motion in Fe-Mn based alloy samples.

Movie S6. Rearrangement of dislocations, and appearance and disappearance of slip steps near a GB at different stages of H desorption from a duplex stainless steel sample.

Movie S7. Molecular dynamics simulation of dislocation evolution during H-charging of a pre-strained polycrystalline Ni sample.

Movie S8. Molecular dynamics simulation of dislocation evolution during relaxing of a pre-strained polycrystalline Ni sample.

Supplementary figures:

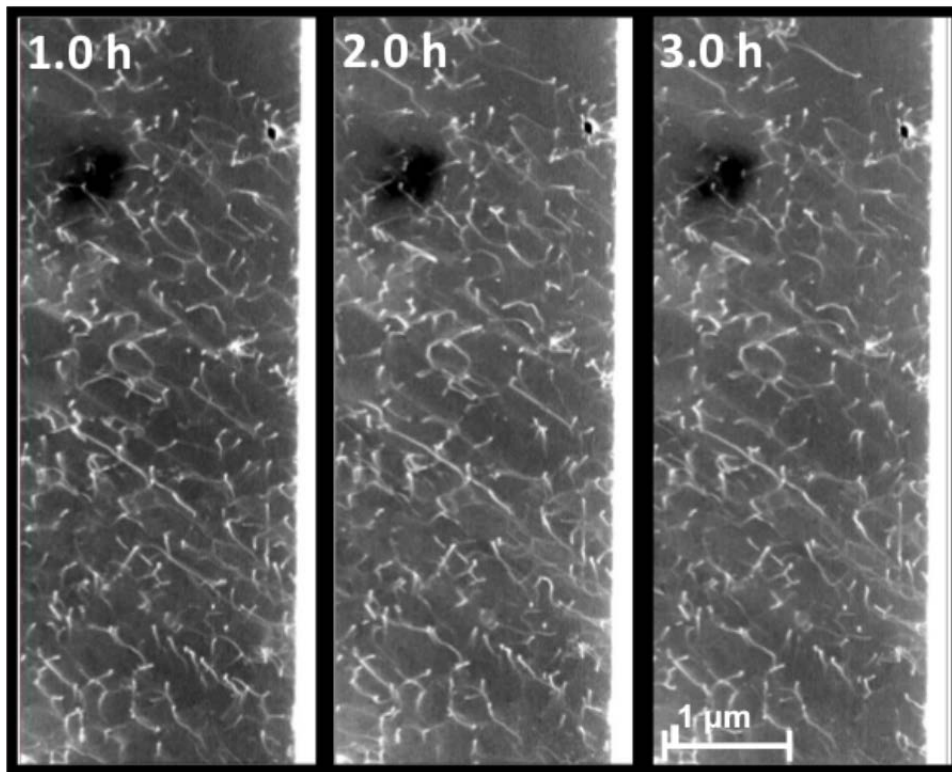


Fig. S1. ECCI micrograph of a dislocation pattern in Fe-Mn based alloy. ECCI micrograph of a dislocation pattern after one, two, and three hours of H desorption. Dislocations rearrange and move during the process.

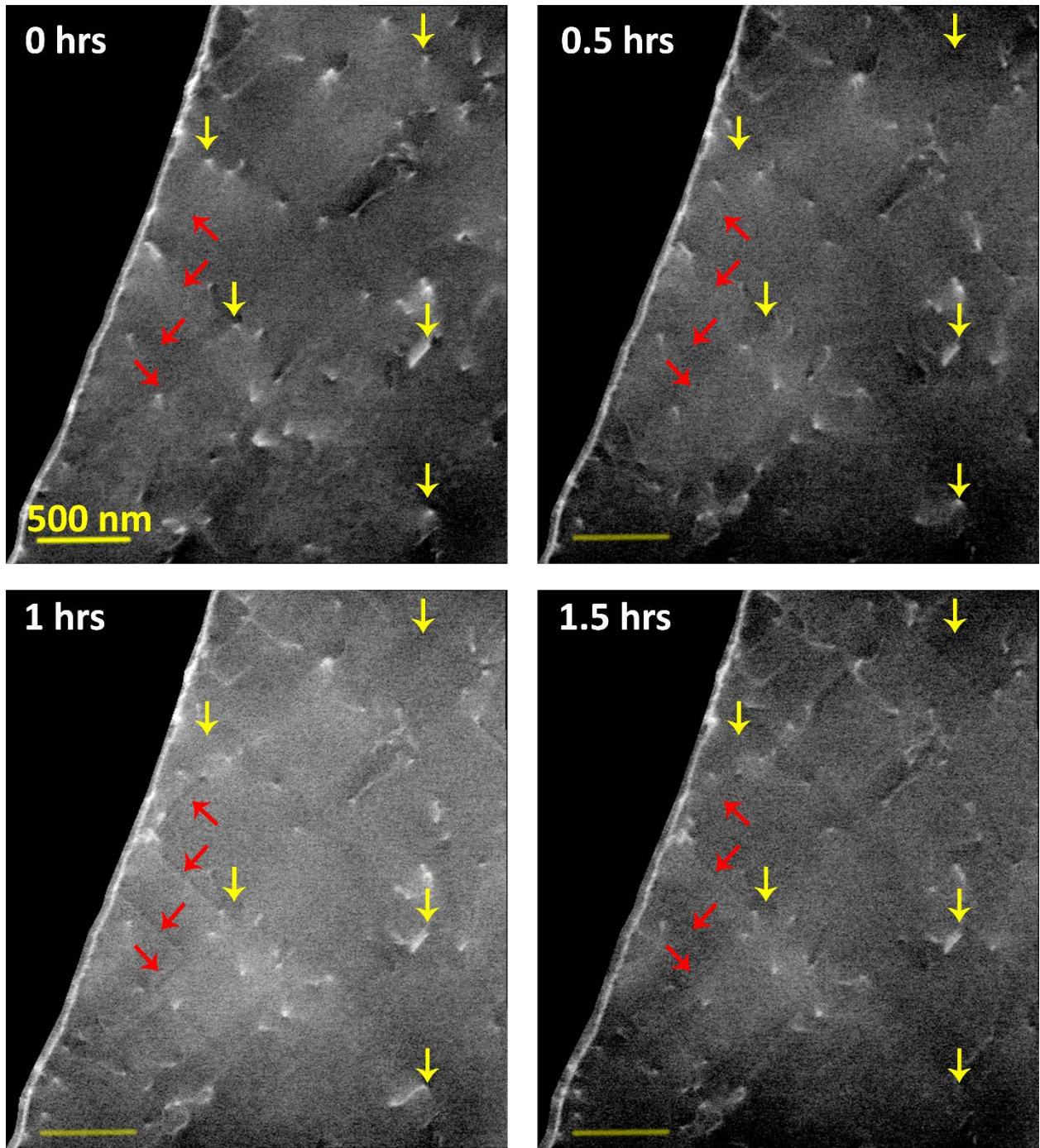


Fig. S2. Dislocation rearrangements and slip-step formations in duplex stainless steel during H-desorption. Yellow and red arrows throughout all four timestamps point towards some of the locations where dislocation motions and slip-steps formation/disappearance occur respectively in the sample.

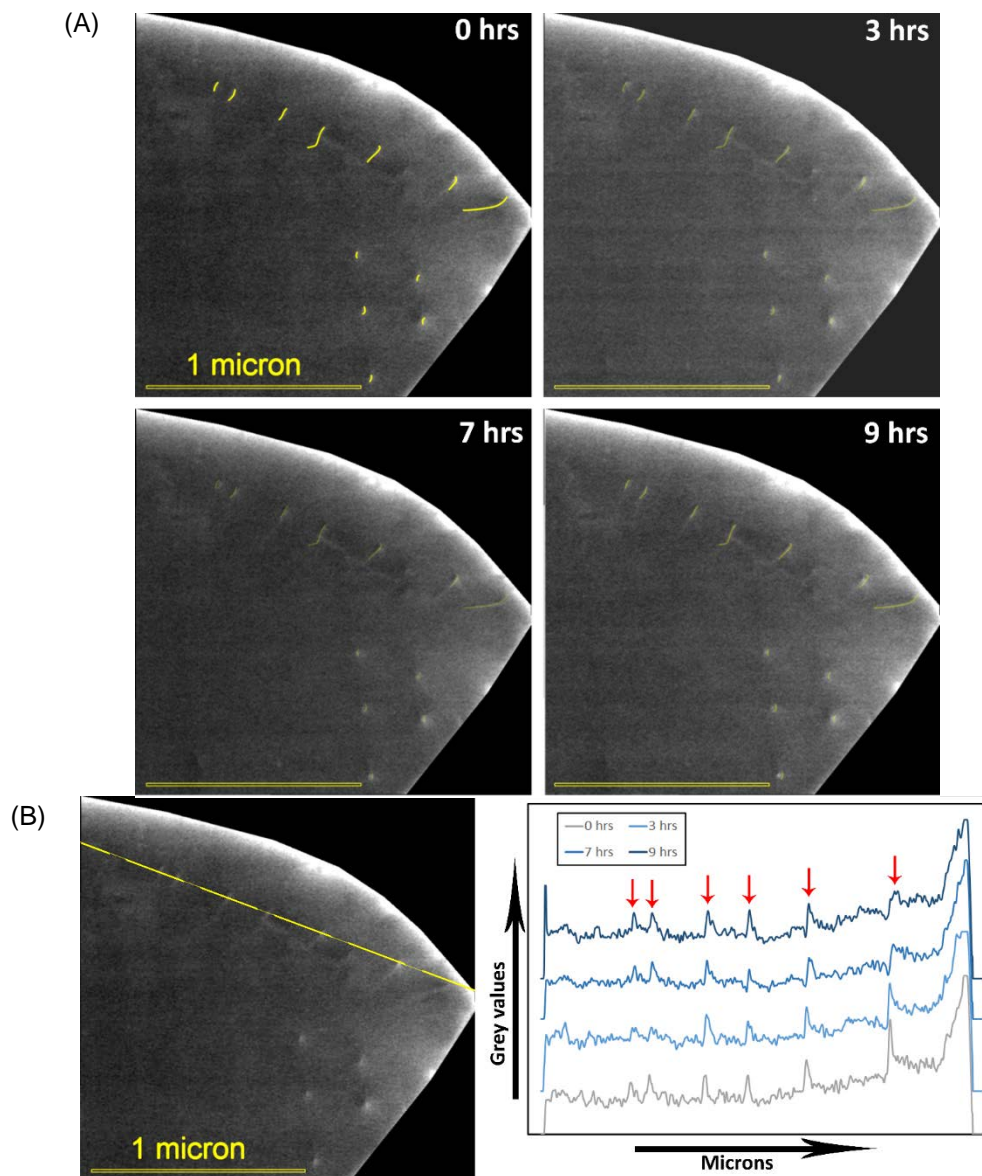


Fig. S3. A planar dislocation pile-up at a GB of Fe-Mn based alloy during 9 hrs ECCI in SEM chamber. (A) The initial dislocation lines (colored in yellow) are motionless during the entirety of the ECCI experiment. This indicates that there are no dislocation motion and slip-step activities in the absence of H. (B) Line profiles of greyscale values across the dislocation pileup (along the yellow dotted line) in Fe-Mn based alloy sample are plotted for ECCI micrographs acquired at four different timestamps. The peak/jump in brightness values corresponds with the presence of dislocation within the ECCI micrograph. The peak locations did not change throughout the 9 hrs of ECCI, indicating that the ECCI technique does not lead to dislocation motions.

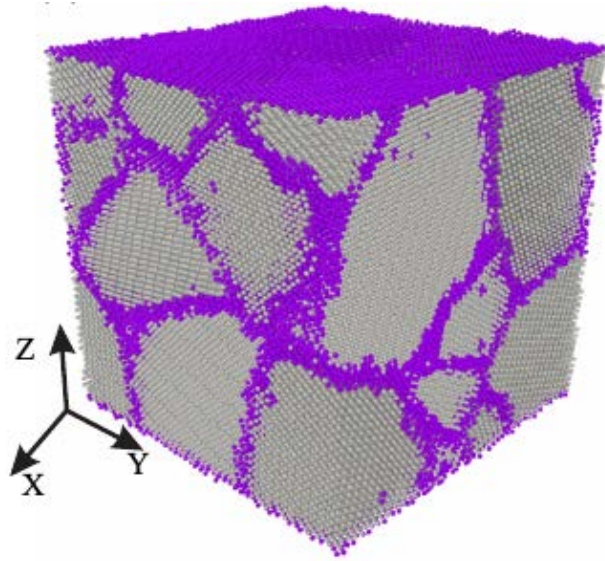


Fig. S4. Polycrystalline Ni sample containing 8 randomly oriented grains used in molecular dynamics simulations.

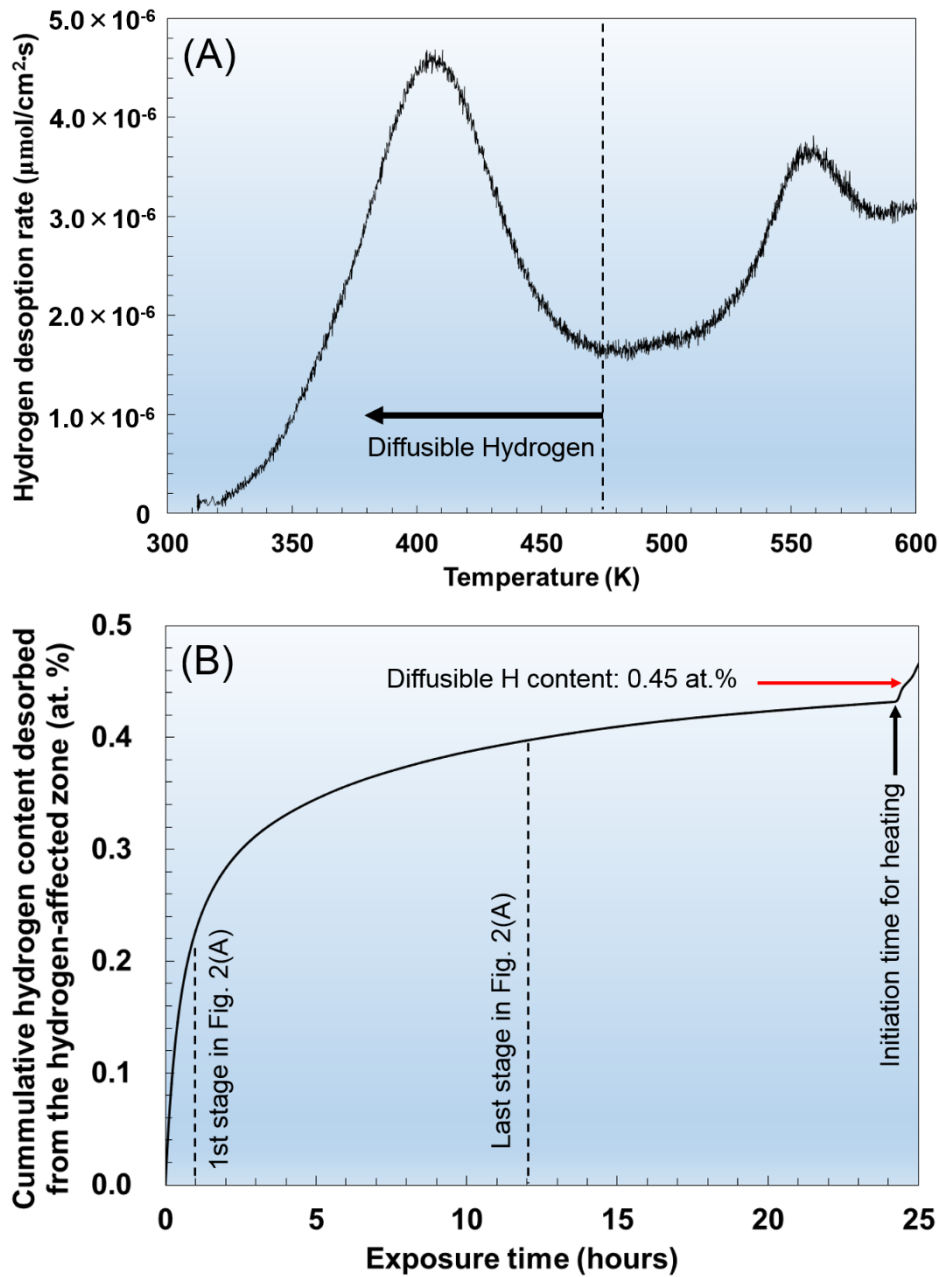


Fig. S5. Measurement of H desorption rate in a mass spectrometer chamber. (A) H desorption rate from the specimen surface plotted against temperature. **(B)** Cumulative H content desorbed from the H-affected zone in a chamber of a mass spectrometer in the same steel as in Fig. 2(A). After the exposure for 24 hours, the specimen was heated up to 600 K at a heating rate of 400 K/h to measure total diffusible H content.

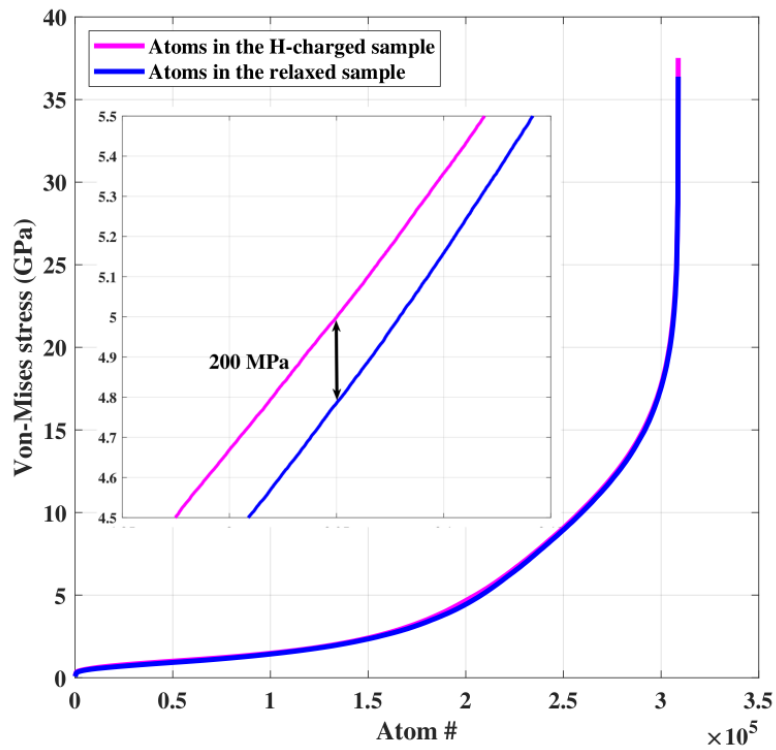


Fig. S6. Atomistic calculation of von Mises stress distribution due to H diffusion in the sample. The von Mises stress distribution for individual atoms before and after H-charging in the sample.

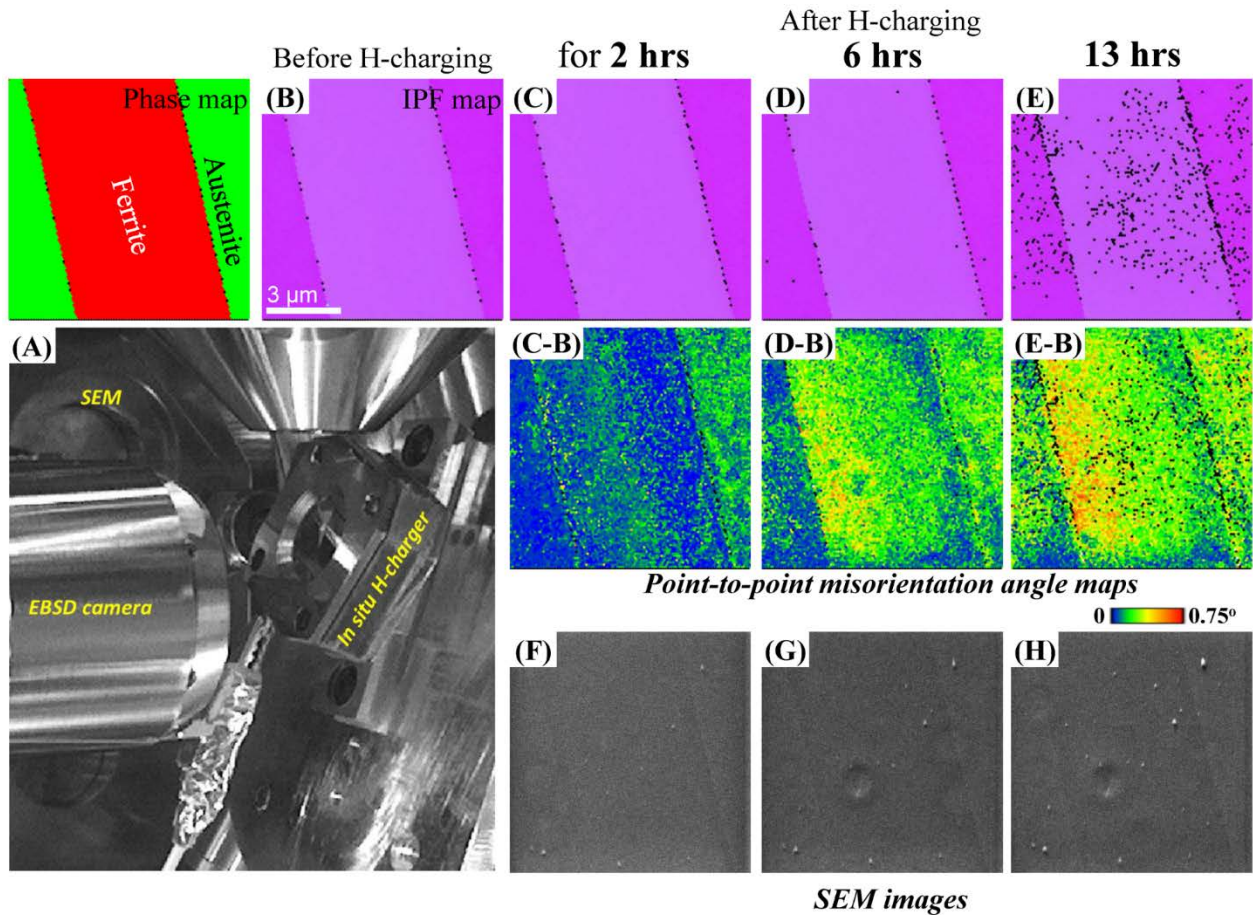


Fig. S7. In-situ EBSD analysis during H-charging of duplex stainless steel. (A) Infrared image inside the chamber with the *in-situ* H-charging setup (“Photo Credit: Jinwoo Kim, MIT”). (B) IPF map of observation region, where two phase boundaries are identified. (C-E) are the IPF maps of the same region after 2 hours, 6 hours, and 13 hours of H-charging, respectively. (F-H) are the SEM images of the same regions. A point-to-point misorientation angle map was created for each time step. The increase in misorientation angles along phase boundaries as a function of H-charging time may reflect an increase in localized stress induced by H-segregation at the boundary.

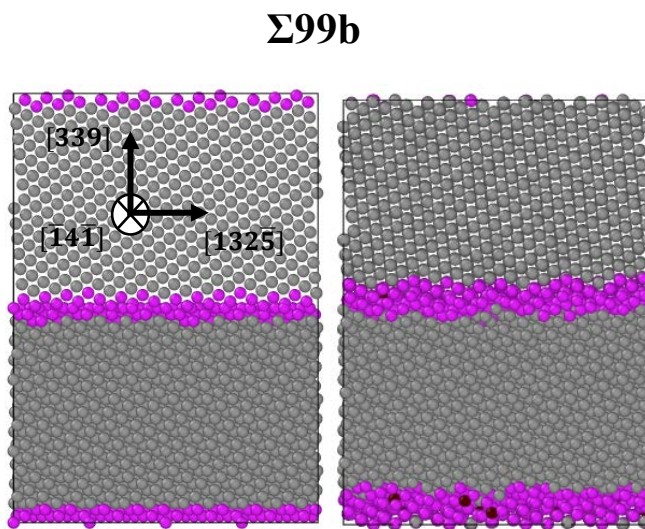
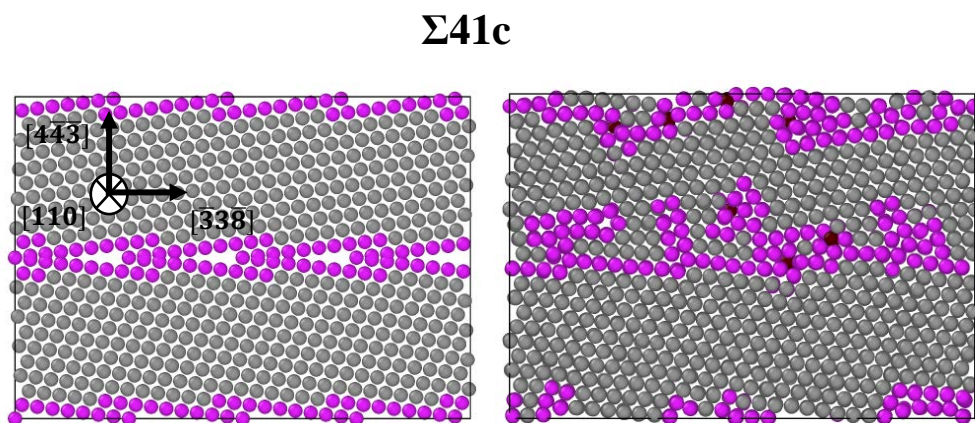
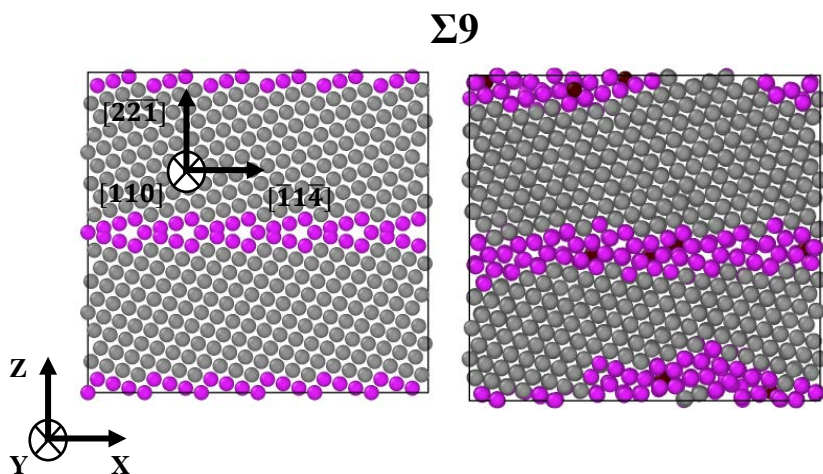


Fig S8. Initial and H-charged Ni $\Sigma 9$, $\Sigma 41c$, and $\Sigma 99b$ symmetric GB structures. In the adopted atom coloring scheme, grey stands for face-centered-cubic atoms, and purple for atoms in GBs. H atoms are colored in red.

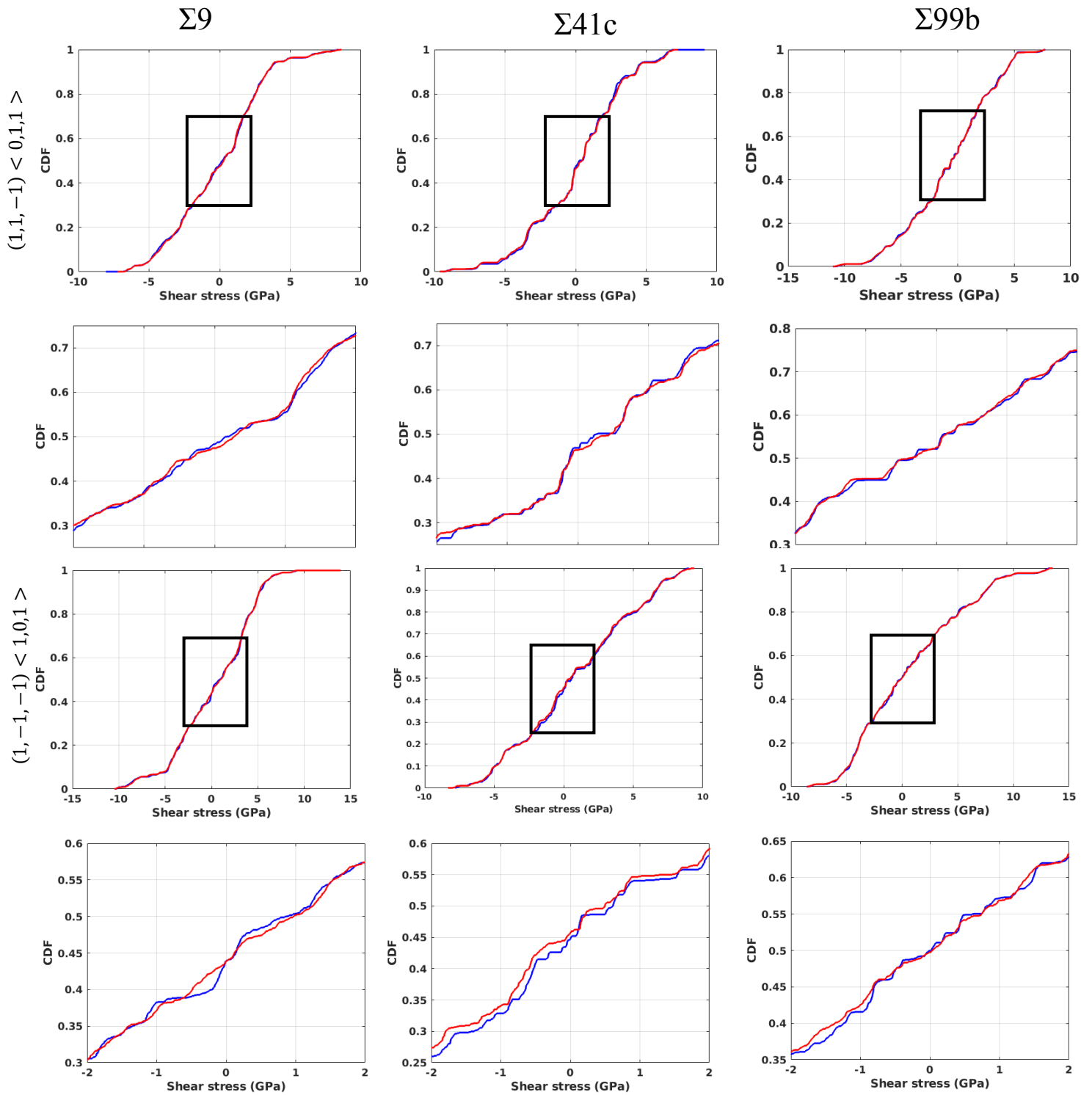


Fig. S9. Cumulative Density Function (CDF) of shear stress in H-charged and free samples along two arbitrary slip directions in fcc Ni sample. The CDF is shown for $(1,1,-1) < 0,1,1 >$ and $(1,-1,-1) < 1,0,1 >$ slip directions and together with the zoomed windows are presented for three different types of GBs ($\Sigma 3$, $\Sigma 41c$, and $\Sigma 99b$). The figures clearly show that H induces change of shear stress ~ 5 -200 MPa along $(1,-1,-1) < 1,0,1 >$ slip direction, and it does not change the shear stress significantly

along $(1,1,-1) \langle 0,1,1 \rangle$ direction, indicating inhomogeneous effects on dislocation motion in the sample.

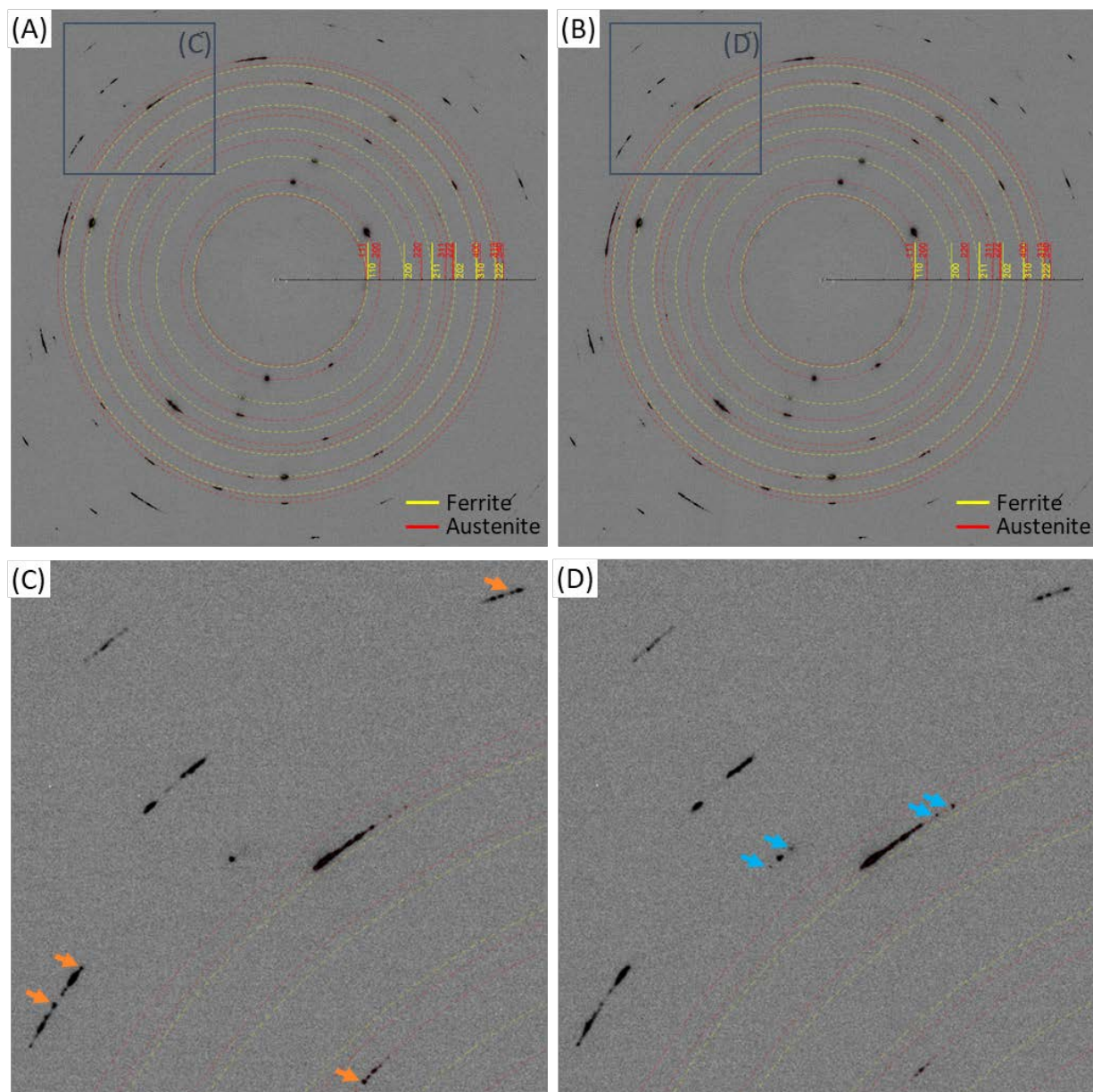


Fig. S10. Synchrotron diffraction pattern of duplex stainless steel. The pattern (A) before H-charging and (B) after 427 min of cathodic H-charging. (C) and (D) show zoomed-in regions indicated in (A) and (B) respectively. Orange arrows in (C) point out the locations where diffraction spots disappear/weaken after H-charging whereas blue arrows in (D) indicate the locations where diffraction spots become stronger.